

Diffraction line profiles of spherical hollow nanocrystals

Emiliano Burrese¹ and Leander Tapfer¹ 

Abstract

An analytical expression of diffraction line profiles of spherical hollow nanocrystals (NCs) is derived. The particular features of the profile lines, enhanced peak tail intensity, are analyzed and discussed as a function of the NC size parameters (outer and inner radius, shell thickness). The explicit formula for the *integral breadth*, the *Fourier particle size*, and the Scherrer constants are also obtained and discussed in detail. The diffraction line profiles of hollow CdS NCs of zincblende and wurtzite crystallographic structure are calculated and compared with Debye scattering profiles. The diffraction profiles of both approaches exhibit an enhanced peak tail intensity that can be considered as a *fingerprint* of the hollow NC structure.

Keywords

Diffraction, nanoscale materials, quantum dots, hollow nanocrystals

Date received: 5 December 2018; accepted: 29 January 2019

Topic: Nanoparticles and Colloids

Topic Editor: Dr Paola Prete

Associate Editor: Dr Paola Prete

Introduction

Recently, hollow NCs are attracting an increased scientific and technological interest due to their intriguing optical, electronic, electro- and photochemical, and catalytic properties that may find use in potential applications in diverse fields such as nanoscale encapsulation and drug delivery, photocatalysis and plasmon photonics, energy storage (anode material in Li-ion batteries), and nanoreactors. Different synthesis approaches for the fabrication of nanoscale hollow structures are reported: Kirkendall cavitation process,^{1–3} template-free hydrothermal method,⁴ template-engaged replacement reactions,⁵ galvanic replacement reaction by combining colloidal synthesis and solid state chemistry,⁶ aminothermal synthesis,⁷ and solvothermal method.⁸

By these synthetic routes, metallic (Co, Au, Ag, Pt),^{2,5,6} semiconductor compound (CoS, CoSe, CdS, SiAlPO),^{2,7} metal oxide (CoO, CuO, TiO₂),^{2,4,8} and carbon-based⁹ hollow NCs were successfully fabricated. However, the crystalline structure may depend on the process parameters

yielding either polycrystalline or monocrystalline hollow nanostructures.³ On the other hand, some synthetic routes^{3,5,7} allow a high control of the NC shell thickness by tuning the process parameters properly.

In order to *visualize* the hollow nanostructure morphology and to determine the microstructural properties (size, shape, crystallinity, etc.), high-resolution transmission electron microscopy techniques (HRTEM, STEM) have been successfully used.^{1–9} However, as for polycrystalline materials, NCs, and colloids, X-ray diffraction methods

¹ ENEA – Italian National Agency for New Technologies, Energy and Sustainable Economic Development, Brindisi Research Centre, Brindisi, Italy

Corresponding author:

Leander Tapfer, ENEA – Italian National Agency for New Technologies, Energy and Sustainable Economic Development, Brindisi Research Centre, Strada Statale 7 “Appia” km. 7+300, 72100 Brindisi, Italy.
Email: leander.tapfer@enea.it



may also be suitable for the microstructural characterization of hollow NCs.

In fact, X-ray scattering methods are experimental tools frequently used to investigate the structural properties and to determine morphological and structural parameters and to evaluate the ordering and architecture of nanoscale materials.¹⁰ In particular, for nanocrystalline materials, X-ray diffraction is a very powerful and nondestructive evaluation tool that provides useful information for a better comprehension and understanding of the functional properties of nanocrystalline materials and that allows to optimize fabrication processes and synthesis procedures.^{11,12}

In most cases, the interpretation of the experimental data is achieved only by modeling of the diffraction profiles. Here it is fundamental to use the correct model for the data analysis. The line shape and width (breadth) of the diffraction peaks depend on several parameters and factors like crystallite shape and size, microdefects, strain, and so on.¹³ In many cases, nanocrystalline particles exhibit a geometrical structure (shape) that reflects their crystallographic structure; the diffraction line profile and breadth are related to the size and shape of the nanocrystallites. Analytical formulae for some particle shapes (spheres, cubes, cylinders, octahedral, tetrahedra) were found and are frequently used.^{14,15}

Therefore, X-ray diffraction is a very powerful method in characterizing quantitatively the shape and size of crystalline nanoparticles (nanopowders, colloidal nanoparticles, nanocomposites, etc.), and the microstructural parameters can be extracted from X-ray diffraction line profiles by pattern decomposition that is still a very frequently used data analysis approach.^{13,16}

In this work, we derive an analytical formula that describes the diffraction (line profile) on hollow spheres, that is, spherical shell NC. In addition, the analytical expressions for integral breadth and Fourier apparent size are derived; as well known, these parameters are usually employed in the pattern decomposition method.^{13,16,17} The diffraction line profile features are discussed as a function of the microstructural parameters (size), and the line profile calculated by the analytical kinematical formula is compared with calculations based on the Debye equation.

Diffraction on hollow spherical nanocrystals

Diffraction line profile

The intensity diffraction line profile of a crystallite of dimension D can be expressed as^{14,15}

$$I(k_s, D) = \frac{1}{V_0} \int_{-\tau}^{+\tau} V(t, D) \cdot e^{-2\pi i k_s t} dt \quad (1)$$

with $k_s = k - k_0 = \frac{2}{\lambda} \cdot (\sin\theta - \sin\theta_0)$, where θ_0 is the Bragg angle and θ is the scattering angle. $V(t, D)$ is the

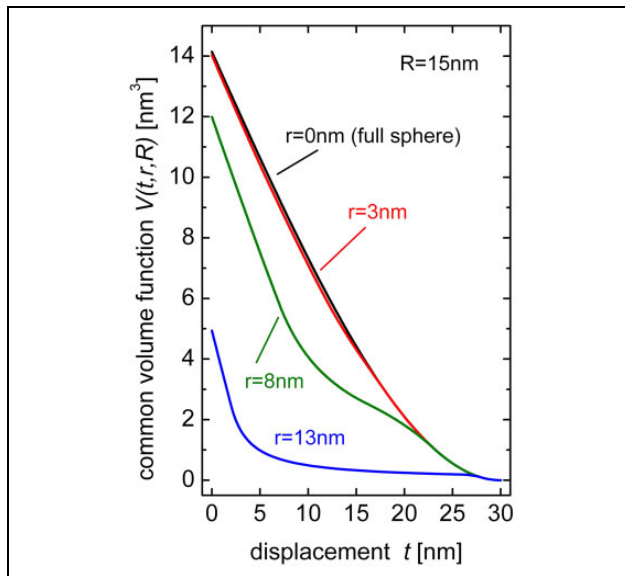


Figure 1. Common volume function $V(t, r, R)$ as a function of the displacement t of a hollow sphere of outer radius $R = 15$ nm and of different inner radius values r . For comparison, the common volume function of a solid sphere with $R = 15$ nm is also shown (black line).

common volume function of the crystallite and the “ghost” crystallite shifted by distance t parallel to the diffraction vector; τ is the value for which $V(t, D) = 0$. $V(t, D)$ is an even function and the common volume function has the boundary conditions

$$\lim_{t \rightarrow 0} V(t, D) = V_0 \quad \text{and} \quad \lim_{t \rightarrow \pm\tau} V(t, D) = 0$$

where V_0 is the volume of the crystallite. In order to solve equation (1), the volume function $V(t, D)$ must be known.

For spherical shell structures, with internal radius r and outer radius R , first the solution of the volume function $V(t, r, R)$, that is, the common volume function of the shell crystallite and the “ghost” crystallite shifted by distance t parallel to the diffraction vector, has to be found. This function has been derived and is given in Appendix 1. Figure 1 shows the function $V(t, r, R)$ for a spherical shell with $R = 15$ nm and $r = 3, 8, \text{ and } 13$ nm, respectively (for comparison, the function of a full sphere of radius $R = 15$ nm is also given).

As a consequence of diffraction in the far-field approximation, the diffraction intensity profile corresponds to the Fourier transform of the crystallite. It follows that the Fourier transform of a crystallite, $V(t, D)$, represents the crystallite size broadened and shape-dependent line profile.

Generally, the shape of crystalline objects is defined geometrically only by the outer surface. Of course, this is not the case of hollow structures that are geometrically defined by an inner surface too. In the case of spherical crystals, the geometrical shape is defined simply by their inner and outer radius (or diameter). Hence, solving equation (1) for spherical shell structures, with inner radius r and outer radius R , we obtain the normalized peak profile function

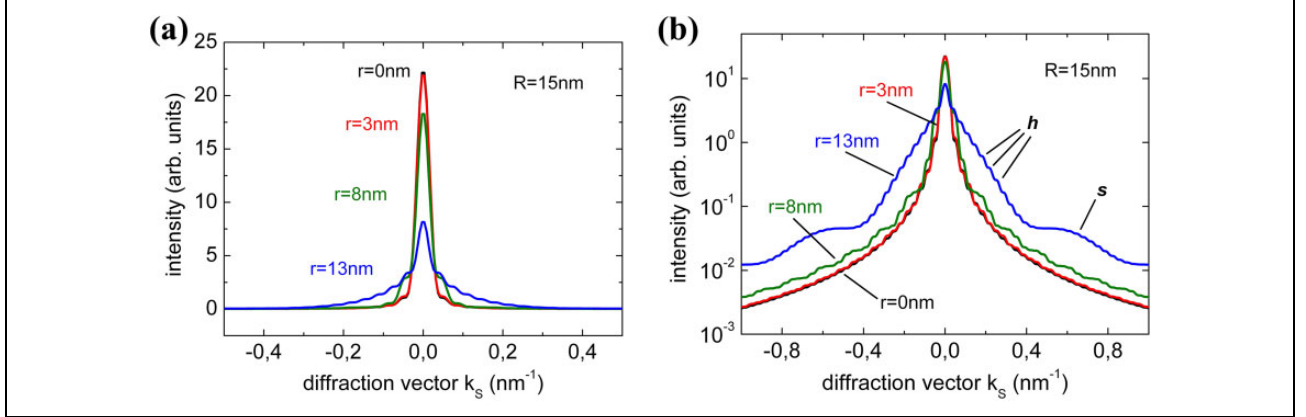


Figure 2. Calculated diffraction profiles of hollow spheres of outer radius $R = 15$ nm and inner radius $r = 3$ nm, 8 nm, and 13 nm, respectively (linear (a) and logarithmic scale (b)). The diffraction profile shape changes with the inner radius r . The peak intensity is reduced while the tails are increased in intensity, and in addition the profile shape exhibits characteristic features that became more pronounced for thin shells (greater inner radius). The profiles for $r = 0$ nm correspond to the full sphere diffraction pattern.

$$I(k_s, r, R) = \frac{1}{(R^3 - r^3) \cdot (2\pi \cdot k_s)^4} \cdot \sum_{j=1}^5 T_j(k_s, r, R) \quad (2)$$

where the terms $T_j(k_s, r, R)$ are given by

$$T_1 = 6(\pi k_s \Delta R)^2 \left[1 - 2(\pi k_s \Delta r)^2 \left(\ln\left(\frac{\Delta r}{\Delta R}\right) - \int_{2\pi k_s \Delta r}^{2\pi k_s \Delta R} \frac{\cos(t) - 1}{t} dt \right) \right]$$

$$T_2 = 3 \left[(\cos(\pi k_s \Delta R))^2 \cdot (1 + 2(\pi k_s \Delta r)^2) - (\cos(\pi k_s \Delta r))^2 \cdot (1 + 2(\pi k_s \Delta R)^2) \right]$$

$$T_3 = \frac{3}{2} \left[\sin(2\pi k_s R)^2 + \sin(2\pi k_s r)^2 \right]$$

$$T_4 = 3\pi k_s \left[\Delta R \cdot \left[1 - 2(\pi k_s \Delta r)^2 \right] \cdot \sin(2\pi k_s \Delta R) - \Delta r \cdot \left[1 - 2(\pi k_s \Delta R)^2 \right] \cdot \sin(2\pi k_s \Delta r) \right]$$

$$T_5 = -3\pi k_s [r \cdot \sin(4\pi k_s r) + R \cdot \sin(4\pi k_s R)]$$

with $\Delta r = R - r$ and $\Delta R = R + r$.

The diffraction profile patterns of hollow nanospheres calculated with equation (2) exhibit peculiar features. Figure 2 shows the diffraction line profiles for a hollow nanosphere of outer radius $R = 15$ nm and different inner radius values $r = 3, 8,$ and 15 nm, for both linear (Figure 2(a)) and logarithmic (Figure 2(b)) scale. For comparison, the diffraction profile of a full sphere with radius $R = 15$ nm ($r = 0$ nm) is also shown (black line). No appreciable difference is

observed between the diffraction profiles of the full sphere and the hollow sphere with $r = 3$ nm. However, with increasing inner radius, the maximum peak intensity decreases as expected (decrease of the scattering volume), while the intensity of the tails increases with increasing hole radius. In particular, for hollow spheres of thin shells, a pronounced broadening and tail intensity enhancement is observed. The central peak width remains essentially the same for full and hollow spheres indicating that the main parameter that

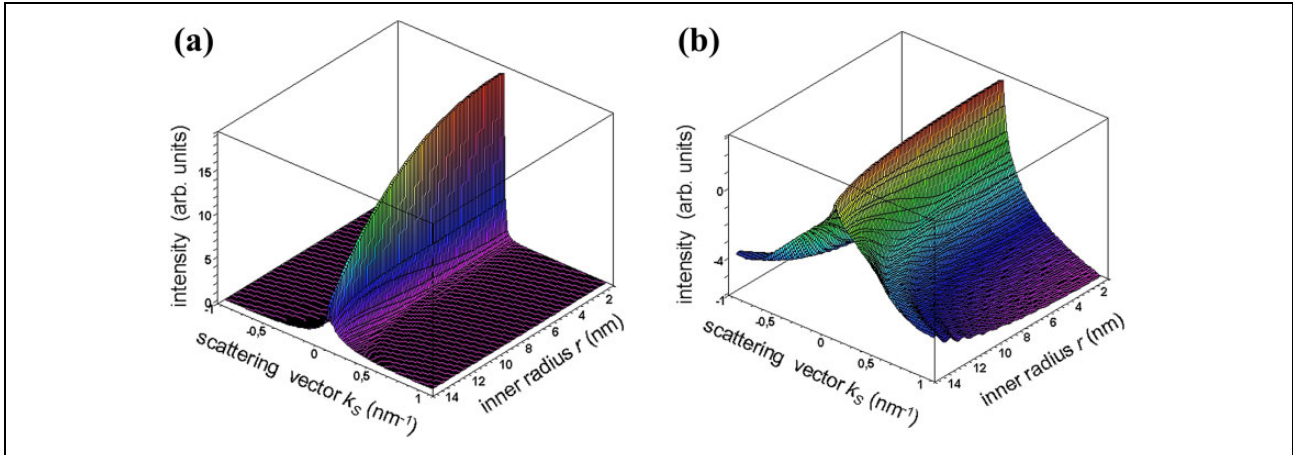


Figure 3. Calculated diffraction profile of a hollow sphere of outer radius $R = 15$ nm. The diffraction profiles are calculated, in accordance with equation (6), as a function of the inner (core) radius values r that vary between 0 nm and 13 nm. The diffraction profile patterns are plotted in linear (a) and logarithmic scale (b).

determines the peak width (FWHM) is the outer radius value R , while the intensity decay of the diffraction peak tails is determined by the inner radius r .

The high frequency intensity oscillations (labeled as “h”) close to the peak maximum are due to the whole dimension of the sphere, that is, the periodicity is related to the outer radius R . In contrast, the low frequency oscillations (labeled as “s”) and their periodicity are related to the inner radius r of the hollow sphere, more precisely the periodicity is related to the shell thickness ($R - r$). From the experimental point of view, in most cases, it will be difficult to observe the intensity oscillations in the diffraction profile curves. But the low frequency oscillations could be observed experimentally similarly to the oscillations of spherical crystallites.

The development of the diffraction profile pattern as a function of the inner radius r (hole) is shown in Figure 3. The outer radius of the hollow sphere is kept constant at $R = 15$ nm, while the inner (core) radius values r vary between 0 nm and 13 nm. The diffraction profile patterns are plotted in linear (Figure 3(a)) and logarithmic scale (Figure 3(b)) since some features are more pronounced in the low intensity range, particularly the intensity decay of the intensity tails.

Crystallite size definitions (integral breadth and Fourier size)

General considerations. The diffraction line profile and peak width depend on the crystallite size. In general, the peak broadening increases with decreasing crystallite size. Pattern decomposition approaches usually employ the integral breadth as a measure of dispersion of the intensity diffraction profile and is defined as the width of a rectangle having the same area and height as

the line profile.^{15,18} The integral breadth due to size effect is given by

$$\beta = \int_{-\tau}^{+\tau} \frac{V_0}{V(t)} dt \quad (3)$$

here, for a spherical shell structure with outer diameter D ($=2R$), $\tau = D$. The integral breadth apparent size ε_β is defined as the reciprocal of the integral breadth, that is, $\varepsilon_\beta = \beta^{-1}$. Hence, the integral breadth apparent size is a volume-weighted size

$$\varepsilon_\beta = \langle D_V \rangle = \int_{-\tau}^{+\tau} \frac{V(t)}{V_0} dt = \frac{2}{V_0} \cdot \int_0^{2R} V(t) dt \quad (4)$$

$\langle D_V \rangle$ is an “apparent” thickness (volume average thickness) of the crystallite along the diffraction vector direction, that is, perpendicular to the diffraction planes.

Crystallite size broadening can also be described in terms of the Fourier coefficients, $A(t)$ in the range $t \in \{0, \tau\}$, given as

$$A(t) = \frac{V(t, r, R)}{V_0} \quad (5)$$

The area-weighted apparent size, or Fourier apparent size, is defined as^{15,16}

$$\varepsilon_\kappa = - \left(\frac{1}{V_0} \cdot \frac{dA(t, r, R)}{dt} \right)^{-1} \Bigg|_{t=0} = - \frac{V_0}{V'(0)} \quad (6)$$

where $V_0/V'(0)$ is the reciprocal of the initial slope ($t = 0$) of the Fourier transform of the diffraction line profile (equation (1)). The Fourier apparent size can be interpreted as the total area of projection of unit volume of the crystallites onto the reflection planes, that is, the apparent “thickness” (area-weighted size) of the

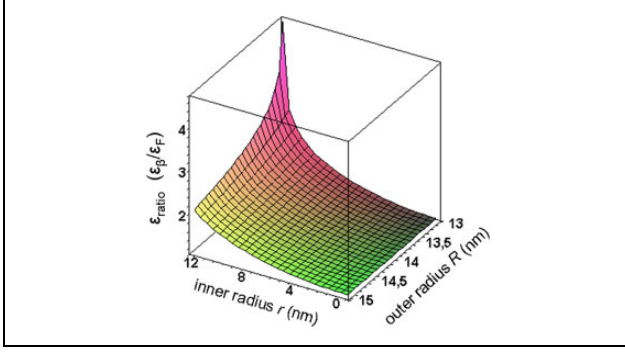


Figure 4. Ratio $\varepsilon_{\text{ratio}}$ of the integral breadth ε_{β} and Fourier apparent size ε_{κ} of the hollow sphere with the same parameters used in Figure 5.

crystallite in the direction of the diffraction vector. The Fourier apparent size does not represent the physical dimension of the crystallite.

Both quantities, ε_{β} and ε_{κ} , are referred to as apparent sizes and are related to the actual physical dimension τ (thickness) of the crystallite along the diffraction vector by the Scherrer constant that must be determined. In general, ε_{β} and ε_{κ} are smaller than the actual size τ and are not equal, that is, the ratio $\varepsilon_{\beta}/\varepsilon_{\kappa} \neq 1$, but in some cases can be as high as 2 depending on the crystallite shape.¹⁶

It should be also recalled that the second derivative of the Fourier transform $V(t, D)$, namely $V''(t, D)$, is proportional to the distribution of the thickness parallel to the direction of the diffraction vector.¹⁴

Integral breadth and Fourier apparent size of spherical hollow NCs. Considering equations (1) and (A9), the integral breadth apparent size (in reciprocal units) due to size

$$\varepsilon_{\beta}(r \rightarrow 0) = \lim_{r \rightarrow 0} \left\{ \frac{3}{4} \frac{(R-r)^2}{(R^3-r^3)} \left[(R+r)^2 \cdot \left(2 - \ln \frac{R-r}{R+r} \right) - 2rR \right] \right\} = \frac{3}{2} R \quad (9)$$

and

$$\varepsilon_{\kappa}(r \rightarrow 0) = \frac{4}{3} \cdot R \quad (10)$$

As already mentioned, generally the values of integral breadth ε_{β} and Fourier apparent size ε_{κ} of a crystallite are not equal and the differences depend also on the crystallite shape. Here, it is interesting to note that the ratio $\varepsilon_{\text{ratio}} = \varepsilon_{\beta}/\varepsilon_{\kappa}$ of hollow spheres depends strongly on the ratio between inner and outer radius (r/R) and the difference between the area-weighted (ε_{κ}) and volume-weighted (ε_{β}) apparent sizes is particularly pronounced for hollow spheres of very thin shells. Figure 4 shows the ratio $\varepsilon_{\text{ratio}}$ of the integral breadth ε_{β} and Fourier apparent size ε_{κ} of the hollow sphere

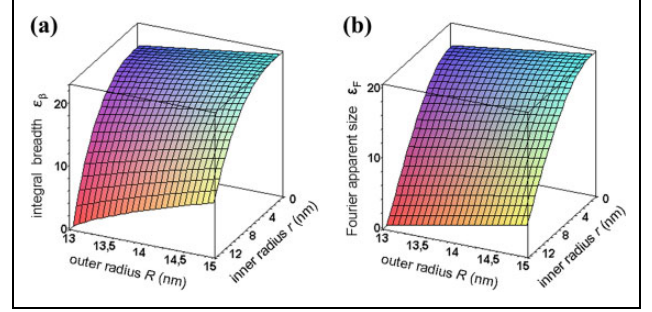


Figure 5. The integral breadth ε_{β} (a) and Fourier apparent size ε_{κ} (b) of a hollow sphere dependence on the outer radius R (range: 13–15 nm) and inner radius r (range: 0–13 nm).

effect of a spherical shell with inner radius r and outer radius R can be determined from equations (4) and (A10) as

$$\varepsilon_{\beta} = \frac{3}{4} \frac{(R-r)^2}{(R^3-r^3)} \left[(R+r)^2 \cdot \left(2 - \ln \frac{R-r}{R+r} \right) - 2rR \right] \quad (7)$$

From equation (6), the Fourier apparent size of a hollow spherical crystallite can be obtained

$$\varepsilon_{\kappa} = \frac{4}{3} \frac{(R^3-r^3)}{(R^2+r^2)} \quad (8)$$

Here, it is interesting to note that the equations of the hollow spherical crystallite yield as limiting case for $r \rightarrow 0$ the known relations of a full spherical NC. In fact, if the inner radius approaches 0, $r \rightarrow 0$, that is, we consider the limiting case of a full sphere, the well-known expressions of spherical crystallites are obtained for the integral breadth and Fourier apparent size

parameters as calculated by equations (7) and (8) and used in Figure 5(a) and (b).

Scherrer constants of spherical hollow NCs. The “true” size p , defined as the cube root of the mean crystallite volume ($p = \sqrt[3]{V_0}$), is related to the apparent size through Scherrer’s equation; $p = K_{\beta} \cdot \varepsilon_{\beta}$ or $p = K_{\kappa} \cdot \varepsilon_{\kappa}$ for the integral breadth or Fourier apparent size, respectively. K_{β} and K_{κ} are the Scherrer constants and are dimensionless numbers. As pointed out by Langford,¹⁶ the concept of “true” size has little physical significance and Scherrer’s approach has been replaced by modern procedures and data analysis.

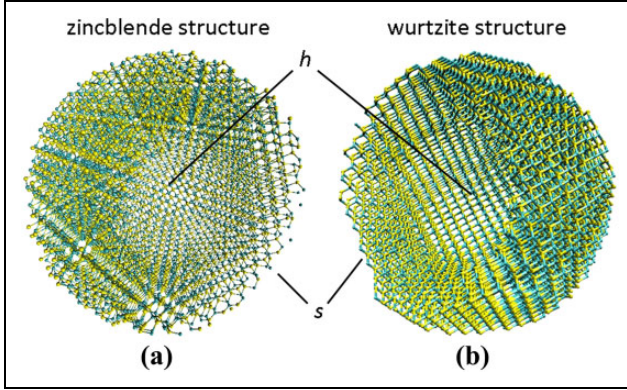


Figure 6. Constructed CdS hollow NC of zb (a) and w structure (b) used for the Debye diffraction calculation; Cd and S atoms are in blue and yellow color, respectively. Here, for a better visualization of the hollow structure (labeled h) of the CdS NCs, part of the shells are removed (labeled s). zb: zincblende; w: wurtzite.

Nevertheless, in the following, we report the analytical expressions for the Scherrer constants obtained by the procedure described in¹⁵

$$K_{\beta} = \frac{\sqrt[3]{\frac{4}{3}\pi(R^3 - r^3)}}{\frac{3}{4} \frac{R-r}{(R+r)^2 - rR} \left[(R+r)^2 \cdot \left(2 - \ln \frac{R-r}{R+r} \right) - 2rR \right]} \quad (11)$$

and

$$K_{\kappa} = \sqrt[3]{\frac{9\pi}{16}} \frac{R^2 + r^2}{\sqrt[3]{(R^3 - r^3)^2}} \quad (12)$$

These expressions are very complex if compared to the Scherrer constants of other crystallites of various shape and depend on crystallite size parameters (here, r and R), similarly to rectangular parallelepiped,¹⁵ cylindrical,¹⁷ and hexagonal¹⁹ crystallites. It can be easily verified that for $r = 0$ (full spherical NC), the Scherrer constants K_{β} and K_{κ} in equations (11) and (12) take the known expressions $\frac{4}{3} \cdot \sqrt[3]{\frac{\pi}{6}}$ and $\sqrt[3]{\frac{9\pi}{16}}$, respectively.¹⁵

Diffraction intensity profiles: A comparison with Debye diffraction

For a comparison of diffraction intensity profiles and powder patterns, we consider a CdS spherical shell NCs of both zincblende (zb) and wurtzite (w) crystallographic structure. Figure 6 shows a schematic representation of the hollow zb and w CdS NCs.

The whole diffraction pattern (powder pattern) that includes all the (hkl) diffraction peaks can be written, considering equation (2), as

$$I_0(k_s, r, R) \approx \sum_{hkl} L \cdot m_{hkl} \cdot |F_{hkl}|^2 \cdot I(k_s, r, R) \quad (13)$$

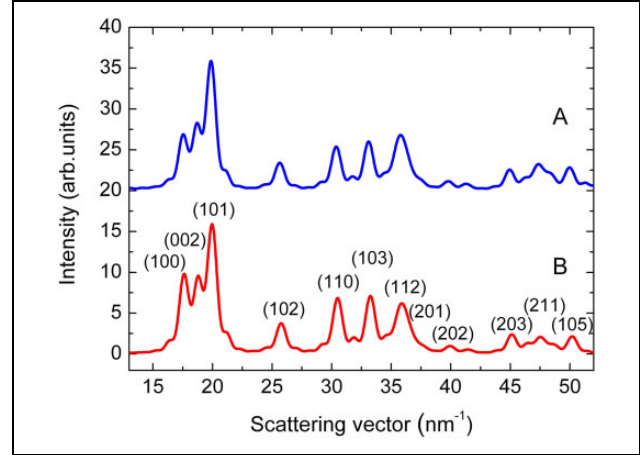


Figure 7. Whole diffraction patterns of hollow CdS NC of w structure calculated with the Debye scattering formula (A) and equation (13) of this work (B). w: wurtzite.

where F_{hkl} and m_{hkl} are, respectively, the structure and multiplicity factors of the hkl reflection. L contains the Lorentz and polarization factors.

For small crystal structures, the calculation of the intensity $I(s)$, with the scattering vector $s = 2\pi \cdot k$, can be also performed considering direct crystalline space, using the Debye scattering equation^{20–22}

$$I(s) = \sum_{i,j=1}^N f_i(s) f_j(s) \frac{\sin(s \cdot r_{ij})}{s \cdot r_{ij}} \quad (14)$$

where r_{jk} is the distance between the i th and j th atoms. In order to obtain the intensity for given values of momentum transfer, the atomic scattering factors $f_i(s)$ are calculated by using the known relation²³

$$f(s) = \sum_{i=1}^4 a_i e^{\left(\frac{-b_i s^2}{16\pi^2}\right)} + c \quad (15)$$

with the corresponding coefficients a_i , b_i , and c for Cd and S atoms, respectively.

First, in order to calculate the Debye diffraction pattern (equation (14)), unrelaxed spherical CdS clusters with zb and w phase were built (Figure 6)²⁴; a first cutoff radius R from the center of the crystal defines the external size whereas a second cutoff radius r corresponds to the internal radius of the hollow cluster. For the spherical NCs of both the crystallographic structures, an outer radius $R = 3.60$ nm has been considered, while an inner radius of $r = 2.00$ nm and $r = 1.95$ nm for the zb and w crystallographic structure, respectively, is considered in order to fulfill the requirements to have a hollow NC constituted by an integer number of atoms.

The whole (powder) diffraction patterns in the range of $k = 13$ nm⁻¹ and 52 nm⁻¹ of a hollow w CdS NC calculated by the Debye scattering equation (curve A) and equation (13) (curve B) are shown in Figure 7. The Miller indices of the diffraction peaks are reported in correspondence of

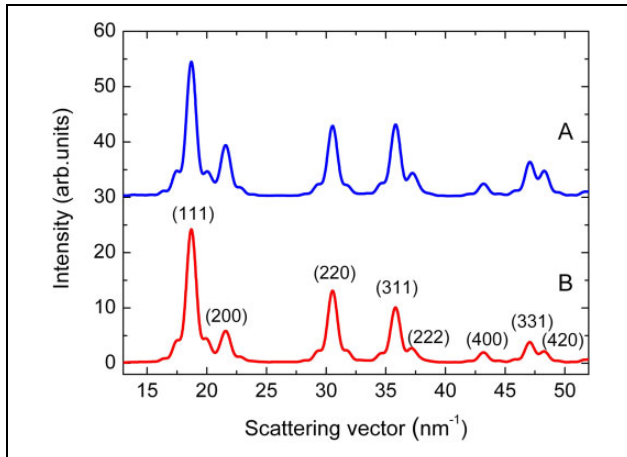


Figure 8. Whole diffraction patterns of hollow CdS NC of *zb* structure calculated with the Debye scattering formula (A) and equation (13) of this work (B). *zb*: zincblende.

curve B. The diffraction peak positions and relative intensity ratios in curve B are in accordance with the data of ICDD n.80-0006²⁵ of bulk *w* CdS. For some diffraction peaks, particularly for (100), (110), (112), and (211), the Debye scattering pattern shows a noticeable discrepancy in the relative intensity ratios.

Similarly, the diffraction patterns of hollow *zb* CdS NC (Figure 8) also show a discrepancy of relative intensity ratios between Debye scattering (curve A in Figure 8) and the scattering curve calculated by equation (13) (curve B in Figure 8). Also here, the diffraction peak positions and relative intensity ratios of curve B are in good agreement with the data of ICDD n.80-0019²⁵ of bulk *zb* CdS.

The intensity ratio differences may be related to the fact that Debye scattering considers the real atomic ordering and configuration on the NC surface (in the case of hollow nanocrystals, also the *interior* surface must be taken into account). On the contrary, the approach used for deriving equation (13) considers the structure factor of the crystallographic unit cell and the specific form factor of the NC; the structure factor is “smeared out homogeneously” over the whole nanocrystal structure and surface effects cannot be taken into account. Similar observations are reported in literature also for full NCs and are particularly noticeable for small-sized NCs (<10 nm),^{26–29} for larger sized NC structures this effect may become negligible.

The most striking features in the diffraction patterns of Figures 8 and 9 are the observed intensity modulations at the peak tails (tail intensity enhancement) that are particularly observable at “isolated” diffraction peaks. The tail intensity enhancement, as discussed above and shown in Figure 2, is a fingerprint of line diffraction profiles of hollow NCs. Figure 9(a) shows the diffraction line profiles of the (220) peak in Figure 8 for the Debye scattering (blue solid line) and the model of this work, equation (13), (red circles). A perfect correspondence of the line profiles is observed. The enhanced tail intensity on both sides of the

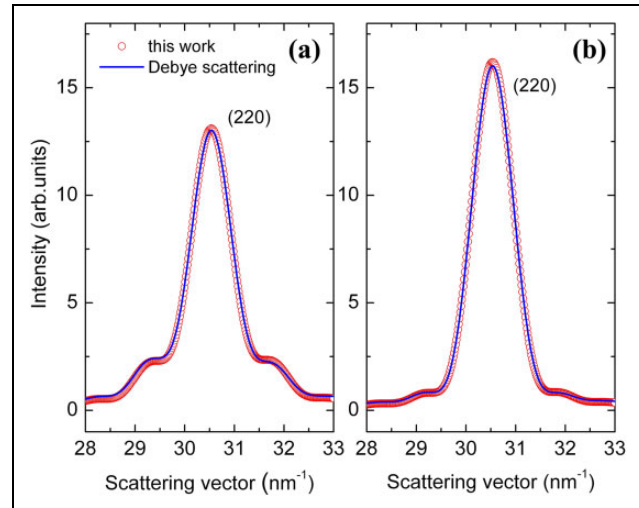


Figure 9. Diffraction line patterns of the (220) peak in Figure 8 for the hollow CdS NC (a) calculated with the Debye scattering formula (blue line) and equation (13) of this work (red circles). For comparison, the (220) diffraction line profile of the full CdS NC ($r = 0$ nm) is also shown (b).

peak is well pronounced and is notably evident if compared with the diffraction line profile of full NCs (Figure 9(b)) calculated with both approaches by taking $r = 0$ nm.

Conclusions

An analytical expression of the diffraction line profile of spherical hollow NCs, with outer and inner radius R and r , respectively, has been derived using Wilson’s approach. In addition, formulae for the integral breadth and Fourier particle size and the Scherrer constants are derived. For $r = 0$, all the formulae lead to the known expressions of full spherical NCs and are discussed as a function of the geometrical (size) parameters.

The diffraction line profiles of spherical hollow NCs exhibit an enhanced intensity at the tails of the diffraction peaks that can be considered as a *fingerprint* of the hollow nanostructure. For comparison, the diffraction profiles of spherical hollow CdS NCs of *zb* and *w* crystallographic structure were compared with the diffraction curves calculated using the Debye scattering equation. Generally, a good correspondence and the same features of enhanced peak tail intensity were observed; differences of some peak intensity ratios (more pronounced at very small particle size <10 nm) are interpreted as a consequence of the atomic ordering and configuration at NC surface that is better and more realistically described in Debye scattering. The analytical expressions derived could be helpful for correct interpretation and quantitative analysis of diffraction data of hollow NC structures of particle size in the range between 10 nm and 100 nm.

Acknowledgement

The Debye scattering computations were performed by using the CRESCO (Computational REsearch centre on COMplex systems)/ENEAGRID High Performance Computing infrastructure

(G. Ponti et al. Proc.Int.Conf. on HPCS 2014, art.no. 6903807, pp. 1030-1033), funded by ENEA and by Italian and European research programmes.


Declaration of conflicting interests

The author(s) declared no potential conflicts of interest with respect to the research, authorship, and/or publication of this article.

Funding

The author(s) received no financial support for the research, authorship, and/or publication of this article.

ORCID iD

Leander Tapfer  <https://orcid.org/0000-0001-5751-0472>

References

1. Yin Y, Rioux RM, Erdonmez CK, et al. Formation of hollow nanocrystals through the nanoscale Kirkendall effect. *Science* 2004; 304(5671): 711–714.
2. Wang W, Dahl M and Yin Y. Hollow nanocrystals through the nanoscale Kirkendall effect. *Chem Mater* 2013; 25(8): 1179–1189.
3. Tianou H, Wang W, Yang X, et al. Inflating hollow nanocrystals through a repeated Kirkendall cavitation process. *Nature Comm* 2017; 8(1): 1261.
4. Jiao S, Lian G, Jing L, et al. Sn-doped rutile TiO₂ hollow nanocrystals with enhanced lithium-ion batteries performance. *ACS Omega* 2018; 3(1): 1329–1337.
5. Sun Y, Mayers BT and Xia Y. Template-engaged replacement reaction: a one-step approach to the large-scale synthesis of metal nanostructures with hollow interiors. *Nano Letters* 2002; 2(5): 481–485.
6. Gonzalez E, Merkoçi F, Arenal R, et al. Enhanced reactivity of high-index surface platinum hollow nanocrystals. *J Mater Chem A* 2016; 4: 200–208.
7. Wang D, Yang M, Zhang W, et al. Hollow nanocrystals of silicoaluminophosphate molecular sieves synthesized by an aminothermal co-templating strategy. *Cryst Eng Comm* 2016; 18(6): 1000–1008.
8. Kobayashi M, Kato H and Kakihana M. Synthesis of titanium dioxide nanocrystals with controlled crystal- and microstructures from titanium complexes. *Nanomater Nanotechnol* 2013; 3: 23.
9. Zou G, Yu D, Lu Y, et al. A self-generated template route to hollow carbon nanospheres in a short time. *Solid State Comm* 2004; 131(12): 749–752.
10. Altamura D, Sibillano T, Siliqi D, et al. Assembled nanostructured architectures studied by grazing incidence X-ray scattering. *Nanomater Nanotechnol* 2012; 2(1): 1–23. DOI: 10.5772/55777.
11. Waseda Y and Muramatsu A. *Morphology control of materials and nanoparticles*. Berlin, Heidelberg, Germany: Springer Verlag Berlin Heidelberg, 2004. DOI: 10.1007/9783662088630.
12. Kasai N and Kakudo M. *X-ray diffraction by macromolecules*. Berlin, Heidelberg, Germany: Springer Verlag Berlin Heidelberg, 2005. DOI: 10.1007/4540283536.
13. Mittemeijer EJ and Welzel U. *Diffraction line profile analysis*. In: Mittemeijer EJ and Welzel U (eds) *Modern diffraction methods*. Weinheim: Wiley-VCH Verlag, 2013. pp. 89–126.
14. Wilson AJC. *X-ray optics*. London: Methuen, 1962.
15. Langford IJ and Wilson AJC. Scherrer after sixty years: a survey and some new results in the determination of crystallite size. *J Appl Cryst* 1978; 11(2): 102–113.
16. Langford IJ. *Use of pattern decomposition or simulation to study microstructure: theoretical considerations* In: Snyder RL, Fiala J and Bunge HJ (eds) *Defect and microstructure analysis by diffraction*. International Union of Crystallography. New York, USA: Oxford University Press, 2000, pp. 59–81. ISBN: 9780198501893.
17. Langford IJ and Louër D. Diffraction line profiles and Scherrer constants for materials with cylindrical crystallites. *J Appl Cryst* 1982; 15: 20–26.
18. Guinier A. *X-ray diffraction in crystals, imperfect crystals and amorphous solids*. New York, USA: Dover Publications, 1994. ISBN 0-486-68011-8.
19. Vargas R, Louër D and Langford IJ. Diffraction line profiles and Scherrer constants for materials with hexagonal crystallites. *J Appl Cryst* 1983; 16: 512–518.
20. Morozumi C and Ritter HL. Calculated powder patterns from very small crystals: body centered cubic cubes. *Acta Cryst* 1953; 6: 588–590.
21. Beyerlein KR. A review of Debye function analysis. *Powder Diff* 2013; 28(suppl S2): S2–S10.
22. Gelisio L and Scardi P. 100 years of Debye's scattering equation. *Acta Cryst* 2016; A72: 608–620.
23. Prince E (ed). *International tables of crystallography Vol. C*. 3rd ed. Bognor Regis, UK: Kluwer Academic Publisher, 2004, pp. 565–581. ISBN 1402019009.
24. Burrelli E and Celino M. Methodological approach to study energetic and structural properties of nanostructured cadmium sulfide by ab-initio molecular dynamics simulations. *Solid State Sci* 2012; 14(5): 567–573.
25. JCPDS—ICDD—International Centre for Diffraction Data, [http://www.icdd.com/\(2000\) CD-Rom](http://www.icdd.com/(2000) CD-Rom)
26. Palosz B, Grzanka E, Gierlotka S, et al. Analysis of short and long range atomic order in nanocrystalline diamonds with application of powder diffractometry. *Z Kristallogr* 2002; 217(10): 497–509.
27. Cervellino A, Giannini C and Guagliardi A. Determination of nanoparticle structure type, size and strain distribution from X-ray data for monatomic f.c.c.-derived non-crystallographic nanoclusters. *J Appl Cryst* 2003; 36: 1148–1158.
28. Kumpf C, Neder RB, Niederdraenk F, et al. Structure determination of CdS and ZnS nanoparticles: direct modeling of synchrotron-radiation diffraction data. *J Chem Phys* 2005; 123: 224707.
29. Kumpf C. Structure determination of very small (1–5 nm) nano-particles. *Appl Phys* 2006; A85(4): 337–343.
30. Salas S, Hille E and Etgen G. *Calculus: one and several variables*. 10th ed. New Jersey, USA: John Wiley & Sons, 2007.

Appendix I

Calculation of the common volume function of a spherical shell

The calculation of the common volume function $V(t)$ has been performed according to the procedure adopted and described by Wilson.¹⁴ Here, $V(t)$ is calculated by solid of revolution method and a washer method that is particularly indicated in the case of hollowed objects.³⁰ As shown in Figure A1, it is convenient to calculate the common volume of a spherical hollow crystal and its “ghost” shifted by t considering the appropriate integration regions, that is, limits of integration. Depending on the magnitude of the inner r and outer radius R of the spherical shell, there are two cases that can be considered: $r < R < 3r$ and $3r < R$. It is obvious that the first case holds for very thin shells, that is, the magnitudes of the inner and outer radius values are very close, while the second case describes spheres with thicker shells (i.e. relatively small hole). For the two cases, integration regions with different integration limits have to be considered. However, the final results are identical as can be easily demonstrated.

In the following, we report for the two cases the expressions of the common volume function for the different integration regions as well as the integration of the common volume function over t , that is, $\int V(t) dt$ that is related to the apparent size of the crystallite (equation (4)).^{14,18}

For the definition of the appropriate integration limits, it is convenient to determine the intersection point x_0 between the outer radius R of the 0-sphere and the inner radius r of the translated t -sphere (“ghost” crystal) for the translation t along the translation axis x

$$x_0 = \frac{R^2 - r^2 + t^2}{2 \cdot t}$$

- i) First, we consider the case of thin shells ($r < R < 3r$) as schematically shown in Figure A1(a).

Integration region 1: $t \in [0, R - r]$

$$\begin{aligned} V_1(t) &= 2\pi \left[\int_{\frac{t}{2}}^R (R^2 - x^2) dx - \int_{\frac{t}{2}}^{r+t} (r^2 - (x-t)^2) dx \right] \\ &= \frac{\pi}{6} \cdot [8(R^3 - r^3) - 6t(R^2 + r^2) + t^3] \end{aligned} \quad (\text{A1})$$

the integration of the volume in the overlapping region 1 yields

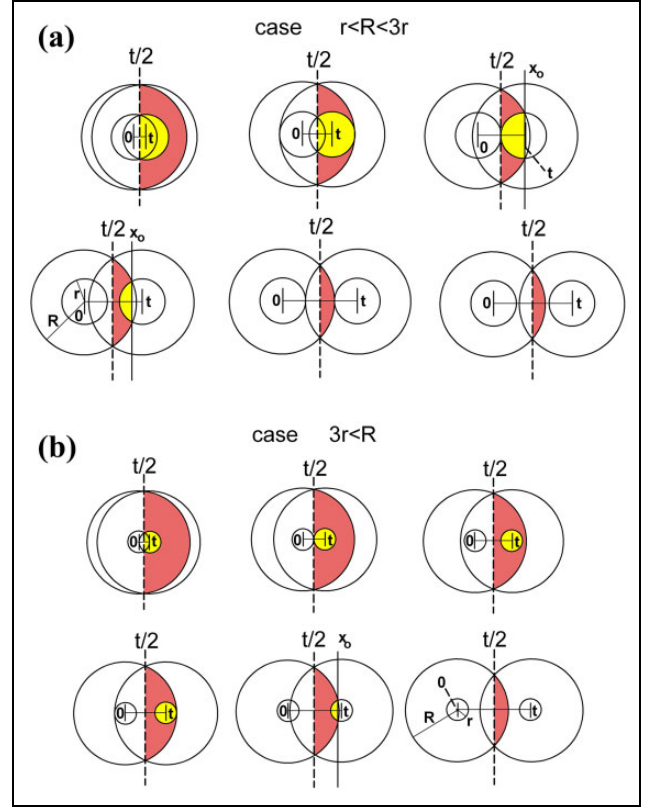


Figure A1. Common volume function calculation with the integration regions for the two possible cases depending on the inner and outer spherical hollow clusters: $r < R < 3r$ (a) and $3r < R$ (b).

$$v_1 = \int_0^{R-r} V_1(t) dt = \frac{\pi}{8} (R-r)^2 (7r^2 + 10r + 7R^2) \quad (\text{A2})$$

Integration region 2: $t \in [R - r, 2r]$

$$\begin{aligned} V_2(t) &= 2\pi \left[\int_{\frac{t}{2}}^{x_0} (R^2 - x^2) dx - \int_{\frac{t}{2}}^{x_0} (r^2 - (x-t)^2) dx \right] \\ &= \frac{\pi}{2} \cdot \left[\frac{(r^2 - R^2)^2}{t} \right] \end{aligned} \quad (\text{A3})$$

with

$$v_2 = \int_{R-r}^{2r} V_2(t) dt = \frac{\pi}{2} (R^2 - r^2)^2 \cdot \ln \left(\frac{2r}{R-r} \right) \quad (\text{A4})$$

Integration region 3: $t \in [2r, R + r]$

$$V_3(t) = 2\pi \left[\int_{\frac{t}{2}}^{x_0} (R^2 - x^2) dx - \int_{t-r}^{x_0} (r^2 - (x-t)^2) dx \right]$$

$$= \frac{\pi}{12} \cdot \left[\frac{6(R^2 - r^2)^2 + 4tr^2(3t - 4r) - t^4}{t} \right] \quad (\text{A5})$$

with

$$v_3 = \int_{2r}^{R+r} V_3(t) dt$$

$$= \frac{\pi}{48} (R-r)^2 \left[\left(24(R+r)^2 \cdot \ln\left(\frac{R+r}{2r}\right) \right) - R^2 - 6rR + 7r^2 \right] \quad (\text{A6})$$

Integration region 4: $t \in [R+r, 2R]$

$$V_4(t) = 2\pi \left[\int_{\frac{t}{2}}^R (R^2 - x^2) dx - \int_{\frac{t}{2}}^{r+t} (r^2 - (x-t)^2) dx \right]$$

$$= \frac{\pi}{6} \cdot [8(R^3 - r^3) - 6t(R^2 + r^2) + t^3] \quad (\text{A7})$$

with

$$v_4 = \int_{r+R}^{2R} V_4(t) dt = \frac{\pi}{48} (7R+r)(R-r)^3 \quad (\text{A8})$$

In summary, for case $r < R < 3r$, the common volume function $V(t, r, R)$ for the four integration regions is

$$V(t, r, R) = \begin{cases} \frac{\pi}{6} \cdot [8(R^3 - r^3) - 6t(R^2 + r^2) + t^3] & \text{if } t \in [0, R-r] \\ \frac{\pi}{2} \cdot \left[\frac{(r^2 - R^2)^2}{t} \right] & \text{if } t \in [R-r, 2r] \\ \frac{\pi}{12} \cdot \left[\frac{6(R^2 - r^2)^2 + 4tr^2(t - 4r) - t^4}{t} \right] & \text{if } t \in [2r, R+r] \\ \frac{\pi}{6} \cdot [8(R^3 - r^3) - 6t(R^2 + r^2) + t^3] & \text{if } t \in [R+r, 2R] \end{cases} \quad (\text{A9})$$

and its integration along t in the scattering direction, v , is

$$v = \sum_{j=1}^4 v_j = \frac{\pi}{2} (R-r)^2 \cdot \left[(R+r)^2 \cdot \left(2 - \ln\left(\frac{R-r}{R+r}\right) \right) - 2rR \right] \quad (\text{A10})$$

For the case of thick shells ($3r < R$), as schematically shown in Figure A1(b), we obtain for the total common volume

function $V(t, r, R)$ and v , that is, the integration of $V(t, r, R)$ along t in the direction of scattering, the following expressions:

For integration region 1: $t \in [0, 2r]$

$$V_1(t) = 2\pi \left[\int_{\frac{t}{2}}^R (R^2 - x^2) dx - \int_{\frac{t}{2}}^{r+t} (r^2 - (x-t)^2) dx \right]$$

$$= \frac{\pi}{6} \cdot [8(R^3 - r^3) - 6t(R^2 + r^2) + t^3] \quad (\text{A11})$$

with the integration of the volume in the overlapping region

$$v_1 = \int_0^{2r} V_1(t) dt = 2\pi r \left(\frac{4}{3} R^3 - 2r^3 - rR^2 \right) \quad (\text{A12})$$

Integration region 2: $t \in [2r, R-r]$

$$V_2(t) = 2\pi \left[\int_{\frac{t}{2}}^R (R^2 - x^2) dx - \int_{t-r}^{t+r} (r^2 - (x-t)^2) dx \right]$$

$$= 2\pi \cdot \left(\frac{2}{3} R^3 - \frac{t}{2} R^2 + \frac{t^3}{24} - \frac{4}{3} r^3 \right) \quad (\text{A13})$$

with

$$v_2 = \int_{2r}^{R-r} V_2(t) dt = \frac{\pi}{48} (R-3r) \cdot (41R^3 - 25rR^2 + 3r^2R - 123r^3) \quad (\text{A14})$$

Integration region 3: $t \in [R-r, R+r]$

$$V_3(t) = 2\pi \left[\int_{\frac{t}{2}}^{x_0} (R^2 - x^2) dx - \int_{t-r}^{x_0} (r^2 - (x-t)^2) dx \right]$$

$$= \frac{\pi}{12} \cdot \left[\frac{6(R^2 - r^2)^2 + 4tr^2(t - 4r) - t^4}{t} \right] \quad (\text{A15})$$

with

$$v_3 = \int_{R-r}^{R+r} V_3(t) dt$$

$$= \frac{\pi}{6} \left[3(R^2 - r^2)^2 \cdot \ln\left(\frac{R+r}{R-r}\right) - r(16r^3 - 11r^2R + R^3) \right] \quad (\text{A16})$$

Integration region 4: $t \in [R+r, 2R]$

$$V_4(t) = 2\pi \int_{\frac{t}{2}}^R (R^2 - x^2) dx = \frac{\pi}{12} \cdot (t + 4R) \cdot (t - 2R)^2 \quad (\text{A17})$$

with

$$v_4 = \int_{r+R}^{2R} V_4(t) dt = \frac{\pi}{4} \left[\frac{1}{12} (7R^4 - r^4) + rR \cdot \left[\frac{3rR}{2} - \frac{5R^2 + r^2}{3} \right] \right] \quad (\text{A18})$$

Finally, for case $3r < R$, the common volume function $V(t, r, R)$ for the four integration regions is

$$V(t, r, R) = \begin{cases} \frac{\pi}{6} \cdot [8(R^3 - r^3) - 6t(R^2 + r^2) + t^3] & \text{if } t \in [0, 2r] \\ 2\pi \cdot \left(\frac{2}{3}R^3 - \frac{t}{2}R^2 + \frac{t^3}{24} - \frac{4}{3}r^3 \right) & \text{if } t \in [2r, R - r] \\ \frac{\pi}{12} \cdot \left[\frac{6(R^2 - r^2)^2 + 4tr^2(t - 4r) - t^4}{t} \right] & \text{if } t \in [R - r, R + r] \\ \frac{\pi}{12} \cdot (t + 4R) \cdot (t - 2R)^2 & \text{if } t \in [R + r, 2R] \end{cases} \quad (\text{A19})$$

and the integration of $V(t, r, R)$ along t in the direction of scattering is

$$v = \sum_{j=1}^4 v_j = \frac{\pi}{2} (R - r)^2 \cdot \left[(R + r)^2 \cdot \left(2 - \ln \left(\frac{R - r}{R + r} \right) \right) - 2rR \right] \quad (\text{A20})$$

Figure A2 shows for comparison the common volume function $V(t, r, R)$ for different NC shell thickness. The

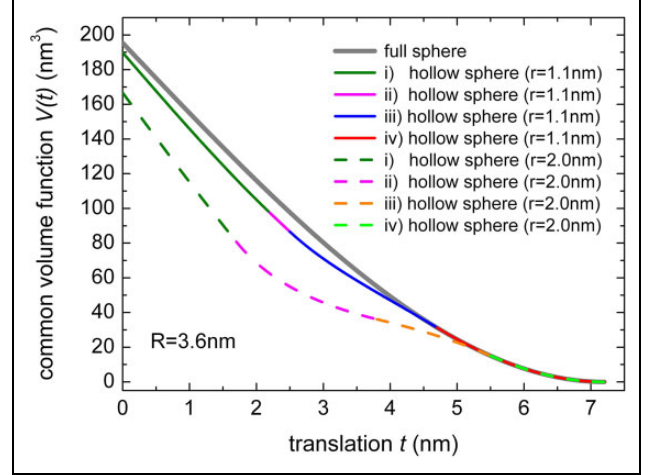


Figure A2. Common volume function $V(t, r, R)$ for spherical hollow NCs with outer radius $R = 3.6$ nm and different NC shell thickness, that is, $r < R < 3r$ (dashed lines) with $r = 2.0$ nm (shell thickness 1.6 nm) and $3r < R$ (solid line) with $r = 1.1$ nm (shell thickness 2.5 nm). The different colors indicate the various integration regions. The grey solid line refers to the full spherical NC with radius $R = 3.6$ nm.

outer radius $R = 3.6$ nm is the same for both cases, $r = 2.0$ nm (dashed lines) with $r < R < 3r$ (corresponds to the example shown in Figure 8) and $r = 1.1$ nm with $3r < R$ (solid line); the different colors indicate the various integration regions. For comparison, also the common volume function of a full spherical NC with radius $R = 3.6$ nm is shown (grey solid line). The deviation of $V(t)$ from a full NC increases with reduced shell thickness and, as expected, the difference is more pronounced at small translation t and reaches 0 for $t = 2R$.